PORE-SCALE STUDY OF THE IMPACT OF FRACTURE AND WETTABILITY ON THE TWO-PHASE FLOW PROPERTIES OF ROCK

DMITRIY SILIN, JONATHAN AJO-FRANKLIN, JOHAN OLAV HELLAND, ESPEN JETTESTUEN, AND DIMITRIOS G. HATZIGNATIOU

Abstract. Fractures and wettability are among other factors that can strongly affect the two-phase flow properties of porous media. Maximal-inscribed spheres (MIS) and finite-difference flow simulations on computer-generated structures mimicking micro-CT images of fractured rock suggest the character of the capillary pressure and relative permeability curves modification by natural or induced fracture and wettability alteration.

1. Introduction

The presence of two or more different immiscible fluids (e.g., water, oil, gas) makes the pore space saturation and fluid flow multiphase. Any oil or gas recovery operation has to deal with two or three-phase flow. The same is true for subsurface injection, for example, for the purpose of CO_2 geologic sequestration. Capillary pressure and relative permeability curves are conventional concepts characterizing the capability of porous materials to store the fluids and the possibility of fluid flow and migration [16]. These curves can be determined from core laboratory experiments. Recently, this traditional approach has been complemented by digital rock methods [18, 21, 22] including pore-network modeling [2, 4, 6–8, 14, 19] and simulations on 2D and 3D micro-tomography data [9, 12, 15, 17]. The method of Maximal Inscribed Spheres (MIS) [23, 24] uses digitized micro-CT data as input information for evaluation of fluid distribution in capillary equilibrium. This method estimates two-phase fluid occupation of the pores, computes capillary pressure and relative permeability curves. The results are in agreement with experimental data [25, 27, 28]. In this study, the MIS method is employed to estimate the impact of natural fractures and wettability on capillary pressure and relative permeability curves. Micro-CT imaging of fractured rock can be difficult. In this study, we generate (via computer) a synthetic material with angular grains. We use micro CT data for samples of Bentheimer sandstone to validate the procedure. After model validation, a fracture is simulated by parting sand grains whose centers are on difference sides of the fracture plane.

2. The method of maximal inscribed spheres

The idea of the MIS method of is simple [23, 27, 28]. In capillary equilibrium, the curvature of the fluid-fluid interfaces is determined by the capillary pressure, which is the pressure difference between wetting and nonwetting fluids. For a given radius of curvature, R, the nonwetting fluid saturation is estimated by evaluating the relative pore volume that can be covered by spheres that can be inscribed in the pores, and whose radii are greater than or equal to R. Such a calculation assumes a zero contact angle at the interface between the solid and the two fluids. In order to account for a non-zero contact angle, the MIS computation is modified. Namely, each inscribed

sphere is blown up by a factor of $(\cos\theta)^{-1}$, where θ, $0 \leq \theta < \pi/2$, is the contact angle, and the nonwetting fluid saturation is evaluated based on these larger spheres. The implementation of this approach almost repeats the zero-contact-angle procedure with an additional verification of connectivity: only the part of the volume that is connected to the original center of each increased spheres is evaluated. For ideally flat pore walls, such a calculation rigorously accounts for the contact angle, see Figure 1. The heterogeneous mineralogy and the roughness of the pore walls practically prohibit rigorous evaluation of the contact angle in a large volume. Thus, the MIS calculation is a compromise between complexity and computational feasibility, and it should be treated as a reasonable first approximation only. Level-set methods (see [11, 20]) are likely to be more accurate in describing the local fluid-fluid interfaces of constant mean curvature. However, level-set methods are computationally demanding. MIS calculations can process gigabytes of data on a desktop-size personal computer. Moreover, the method can reproduce the two-phase fluid distribution observed in micro-CT data and reasonably predict the capillary pressure curves [27].
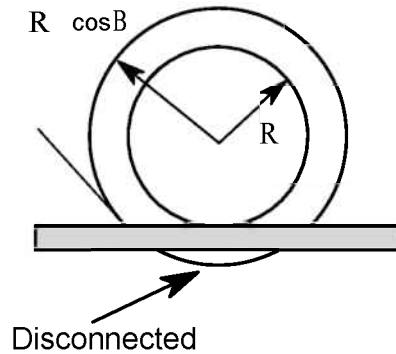

Figure 1. Modeling non-zero contact angle: connectivity needs to be checked after stretching an inscribed sphere by a factor of $\cos\theta^{-1}$. If detected, the disconnected part are removed.

Evaluation of the relative permeability at a given fluid saturation requires flow simulations. To simulate creeping flow, we employ a finite difference projection method of solving Stokes equations [5]. The pressure gradient is imposed by Dirichlet boundary conditions on two opposite facets of the cubic sample, whereas the lateral boundaries are closed. No-slip conditions are imposed on all solid-void boundaries except those constraining the entire sample. Averaged flow velocity field defines the Darcy velocity. The latter is not necessarily aligned with the pressure gradient due to local anisotropy. Flow simulations for three orthogonal pressure gradients yield an estimate of the tensor of permeability. The mean value of the diagonal elements, which is invariant with respect to a rotation of coordinates, estimates the scalar sample permeability. Evaluation of the permeability for each fluid phase at a given saturation, scaled by the absolute permeability of the medium, yields the coefficient of relative permeability values. A relative permeability curve is produced by plotting these values against the respective saturations.

The no-slip condition at fluid-fluid interfaces is a simplification. We justify it by remarking that Darcy velocity is usually determined by the most intense flow paths. The flow path width is determined by the curvature of the interface, that is, by the capillary pressure. For the nonwetting fluid, the wide flow path means that the wetting fluid is pushed to the corners and crevices of the pore space. In particular, if both fluids had similar viscosities, the viscous friction constraining the flow of the non-wetting fluid is expected to be less than that imposed on the

flow of the wetting fluid. In other words, it is assumed that in each individual flow path, one fluid is more mobile than the other. This assumption is a simplification and it restricts applicability of the results. For example, it may be inappropriate for two-phase countercurrent flow.

3. Digital Data

Segmented micron-scale-resolution computed tomography 3D images are the input data for the flow and MIS simulations. The fractured medium for this study was computer-generated using QHull codes [3]. Holtzman et al [10] simulated compaction of a pack of spherical grains. The grain centers produced by this simulation were used to compute a Voronoi tessellation. The derived granular structure consists of polyhedral grains filling the entire volume. Each grain is an intersection of half-planes, where each half-plane is defined by its outer normal and a scalar offset. To mimic the natural rock structure, the grains were shrunk and randomly rotated relative to the respective centers. To model a fracture, we first selected a fracture plane, which is described by its normal and offset. Then, some grains were translated at a fixed distance along the normal direction. The criterion for shifting was based on the grain's Voronoi center position relative to the plane. In other words, all grains were moved away from the plane at a given fixed distance, so that the grains on different sides of the plane were moved in the opposite directions. Figure 2 shows an example of structures obtained by the described procedure. The left-hand image displays a medium without a crack, whereas the one on the right-hand side displays a computer-generated fracture. Note that the fracture-plane orientation is not aligned with any one of the coordinate axes.

To extract a digital image, we define each voxel of the discretized space as solid or pore, depending on whether or not the voxel's center is inside one of the grains. Depending on the chosen resolution, the number of voxels can be different. To test the sensitivity of simulations to the resolution of the image, the geometrical structures shown in Figure 2 were discretized at two res- olutions. The coarser image has dimensions 150 × 150 × 150, whereas the dimensions of the finer one are 300 × 300 × 300. Voxel-counting estimates of porosity were 14% for the nonfractured structure, and 22% for the fractured one. The variations in porosity estimates with respect to the resolution were small: they did not affect the first three significant digits. This stability of segmentation can be explained by the absence of microporosity in the computer-generated samples shown in Figure 2. For natural rock, the presence of small clay particles in some pores may increase the sensitivity of segmentation to the resolution of the image.

The fracture walls in the structure shown in the right-hand side image of Figure 2 are rough, due to the grain corners sticking out into the aperture. Flow simulations, however, show that the fluid velocity inside the crack is much higher than in the intergranular pores (Figure 3).

Figure 4 shows a gray-scale micro-CT image of a Bentheimer sandstone sample generated at the Advanced Light Source facility (ALS) at Lawrence Berkeley National Laboratory (LBNL). Voxel size for this image is 4.42 microns. The lighter gray color indicates higher density. Visually, the light-gray grains are distinct from the darker intergranular space. Although it is difficult to evaluate how well the computer-generated images mimic the real rock geometry, there is visual similarity between the natural sample in Figure 4 and computer-generated data shown in Figure 2. The resemblance between the MIS-calculated relative permeability curves evaluated for the computer-generated samples shown in Figure 2 and Bentheimer data displayed in Figure 4 confirms this visual similarity (see next section).
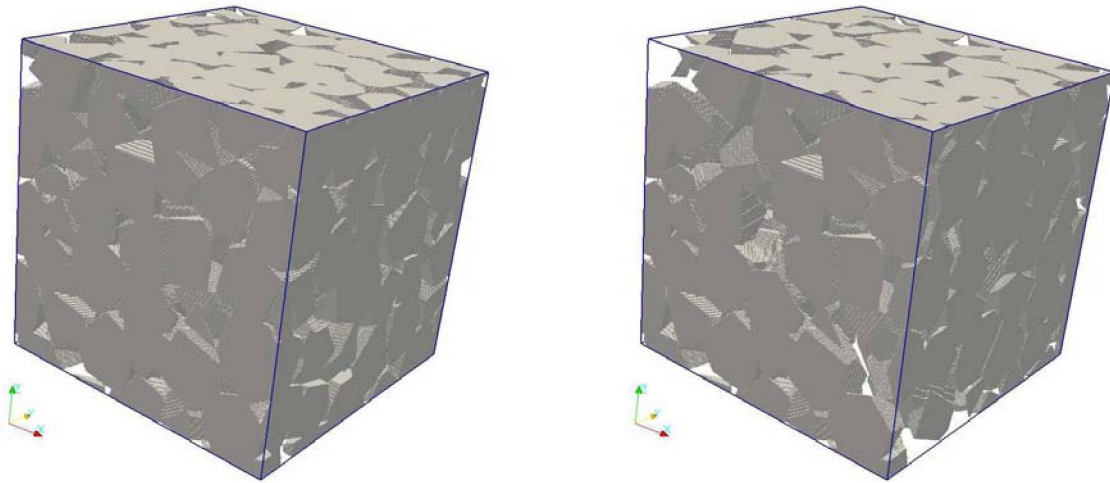
Figure 2. Digitized computer-generated porous structure. The fracture visible on the right-hand side image was generated by a parallel shift of some grains.
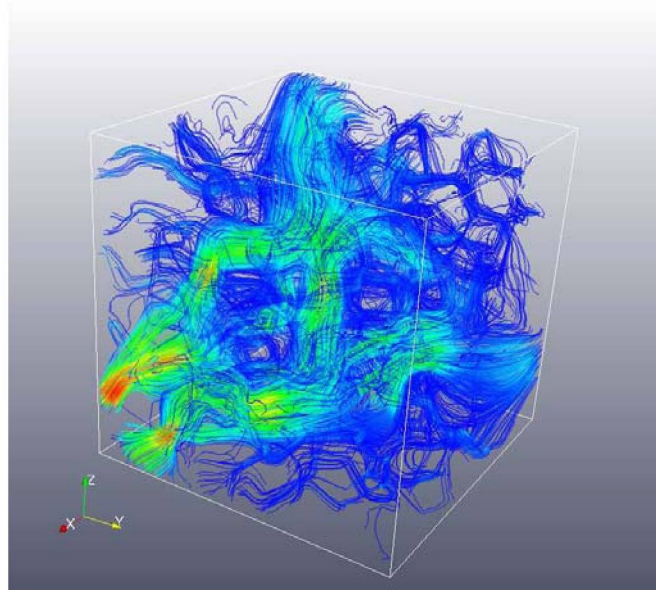

Figure 3. Flow streamlines show much higher flow velocity inside the crack. The warmer color indicates higher flow velocity. The orientation of the structures displayed in Figure 2 was modified to better display flow in the fracture.

4. Results and discussion

The visual similarity between computer-generated unfractured porous medium shown in Figure 2 and the Bentheimer sandstone displayed in Figure 4 is confirmed by the MIS calculations. Figure 5 shows a comparison between the respective invasion capillary pressure curves in the same axes. The gray-scale image in Figure 4 was segmented using thresholding followed by filtering the noise in the output. The segmentation procedure is described in [26].
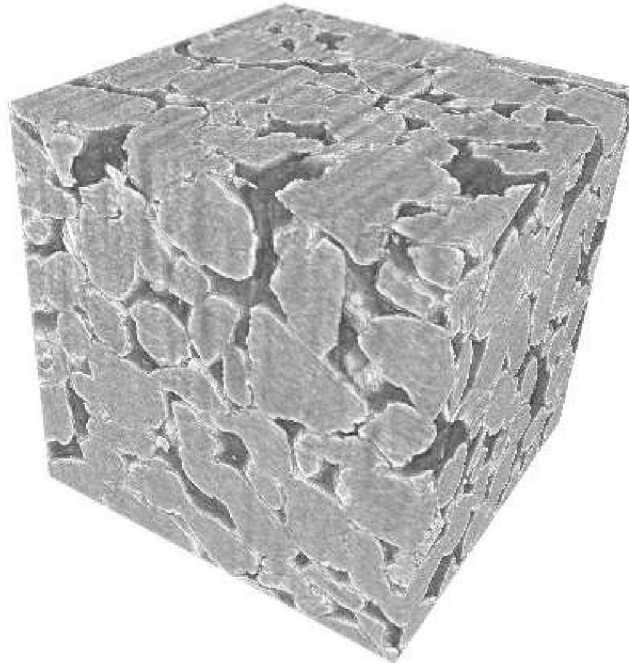
Figure 4. Gray-scale 750×750×750 voxels image of Bentheimer sandstone obtained at the Advanced Light Source Facility at LBNL. Voxel size is 4.42 micron.

The capillary pressure plots are dimensionless, which means that the unit of length is one voxel size, and the interfacial tension coefficient is equal to one. To convert the results into physically meaningful data, the dimensionless values have to scaled by a factor equal to the ratio of the surface tension coefficient to the image resolution.

Figures 6 and 7 show the results from evaluating the dimensionless capillary pressure curves at different image resolutions and contact angles. All cases demonstrate robustness of the algorithm output with respect to the resolution: doubling the number of voxels has little effect on the capillary pressure evaluation except for the very low wetting-phase saturations. Such MIS calculation stability with respect to the quality of the image was observed previously [23, 27, 28]. However, the results can be uncertain for the portion of the capillary-pressure curve corresponding to low wetting-fluid saturations. At a high capillary pressure, the curvature of the fluid-fluid interface is large. Due to the limitations of resolution, MIS calculations may become unreliable.

For the same contact angle, the entry pressure for the fractured medium is lower than that for the porous matrix. This observation is physically sensible and well known. In many cases, if water, oil, and gas share the pore space, gas is the most nonwetting fluid. Thus, the injected gas will likely follow preferential flow pathways in the fractures rather than uniformly sweep large volumes. The viscosity of carbon dioxide, even in a supercritical state, is much lower than that of other reservoir fluids. Therefore, the preferential flow through the formation fractures is likely to be enhanced by the relatively high gas mobility. High injection pressure is likely to propagate through the network of fractures by pressure diffusion. Consequently, the spreading gas plume may bypass the matrix porosity due to the high capillary barrier. This phenomenon is likely to have a stronger effect in tight reservoirs, with low matrix permeability.

The argument in the above paragraph relies on capillary-pressure equilibrium. This equilibrium can shift for various reasons. For example, the interfacial tension coefficient can
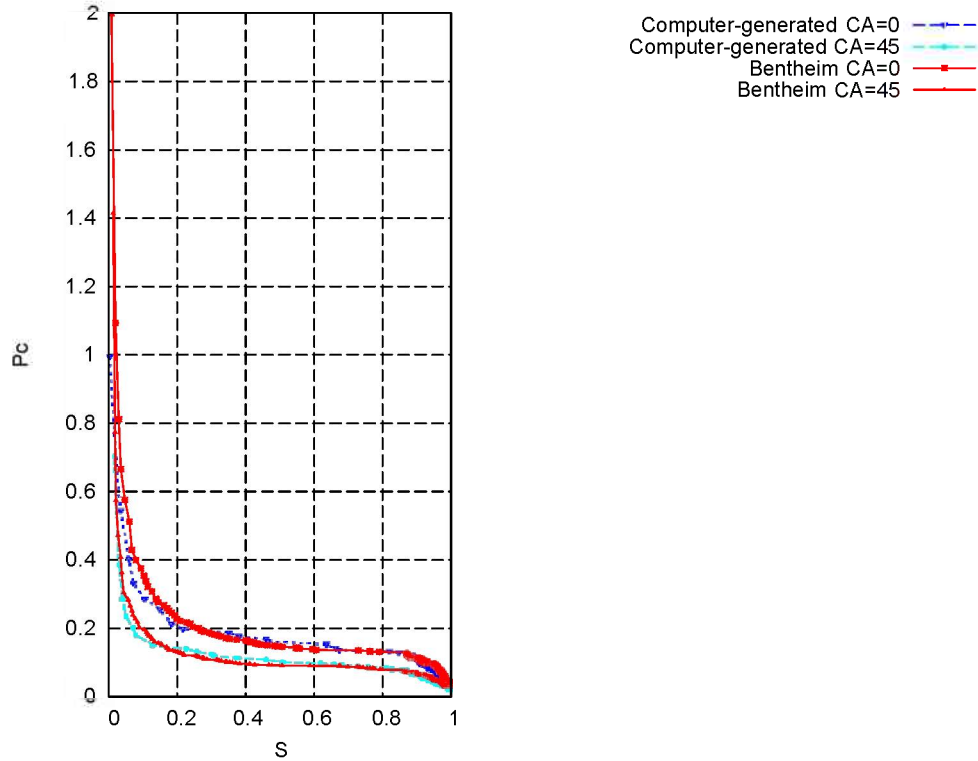
Figure 5. Dimensionless capillary pressure evaluated from images of computer-generated and natural rock samples.

change due to chemical reactions and/or temperature conditions. Rock wettability also can change over time by aging. The plots in Figures 6 and 7 show that the transition from a completely wet environment ($\theta = 0$) to a mixed-wet one ($\theta = 45°$) can significantly reduce the matrix entry capillary pressure. Simulations suggest, though, that a lower matrix entry capillary pressure due to lower affinity to the wetting fluid is insufficient to equalize it with the entry capillary pressure of fractures. Thus, the pattern of preferential gas flow in fractures is likely to be preserved in a wide range of partial wettabilities.

4.1. The $\cos\theta$ factor for capillary pressure. In the literature, the impact of wettability on capillary pressure is usually accounted for by an additional factor of $\cos\theta$ in the expression for capillary pressure through the Leverett's J-function [13]. In the laboratory, verification of this simple rule is difficult, since natural rock usually includes numerous minerals, and the contact angle for one mineral is most likely different for another. Additionally, the roughness of the solid surface can significantly affect the apparent contact angle, so that the latter is not necessarily the same as the contact angle measured under idealized laboratory conditions with a clean, polished solid surface [1]. The plot in Figure 8 suggests that such simple rescaling might be an oversimplification. The circles have coordinates of the invasion capillary pressure evaluated for the same saturations for $\theta = 0$ and $\theta = 45°$ contact angles. The straight line is where all the points should be if the $\cos\theta$-correction factor were applied. The pattern of the deviation from straight line is different for evaluation of drainage and imbibition capillary pressure curves—see Figure 8 A,B. We attribute this observation of high entry capillary-pressure sensitivity to
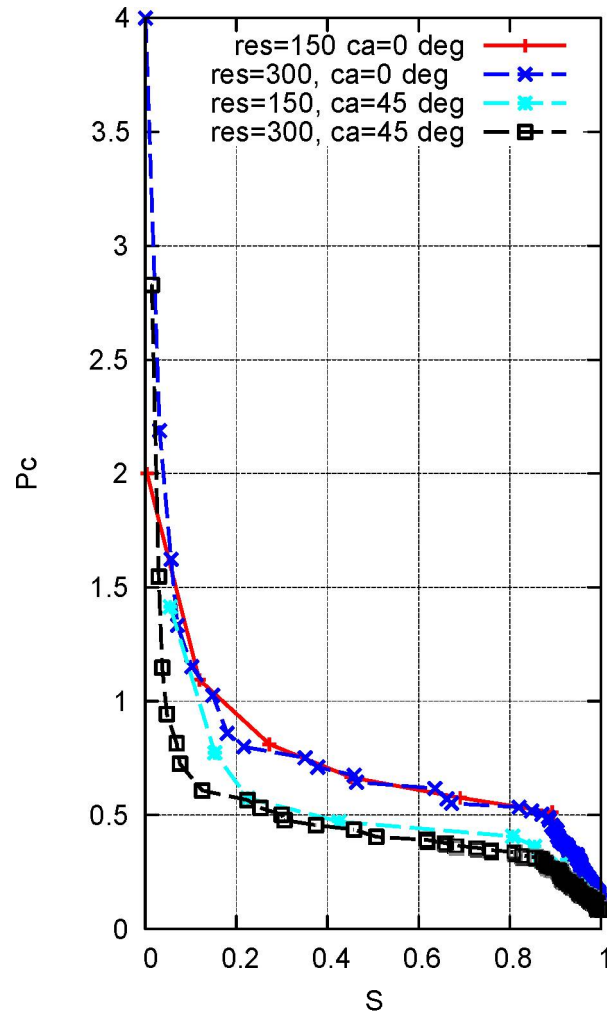
Figure 6. Invasion capillary pressure curves evaluated for different wettability conditions in an unfractured domain.

contact-angle variations. The capillary-equilibrium fluid distribution beyond the entry pressure is less dependent on the wettability of the rock.

Modeling offers an opportunity to run simulations assuming an idealized material with a uniform contact angle. Figure 10 shows relative permeability curves evaluated for Bentheimer CT data for zero and 45° contact angles. The drainage relative permeability curves are shown as dashed lines, and the circles show the computed data points. The solid-line curves evaluate imbibition relative permeabilities. Figure 9 shows relative permeability curves evaluated for a computer-generated medium. A comparison between plots in Figures 10 and 9 suggests similar trends in the modification of computed relative permeability curves by changing contact angle. The difference between the result obtained for zero and non-zero contact angles is not dramatic. Such a difference is more noticeable in results of computations for fractured media (see below).

4.2. Fracture and relative permeability. The presence of a fracture in the same sample dramatically affects relative permeability curves. Figures 9 and 11 show simulation results for
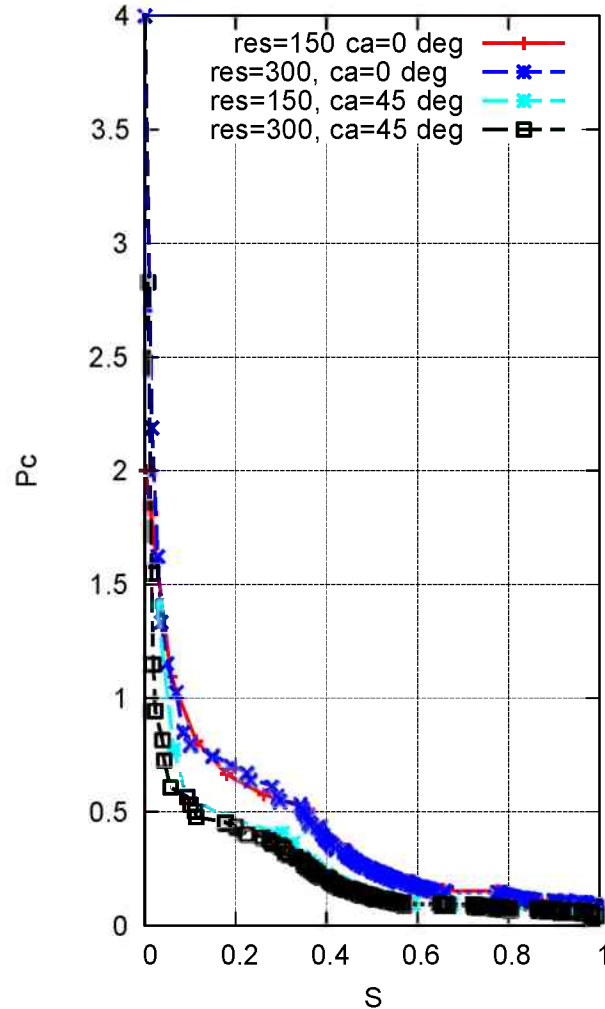
Figure 7. Invasion capillary pressure curves evaluated for different wettability conditions for a sample with fracture.

a 150-cubed discretization of the medium from Figure 2. The solid lines show relative permeabilities evaluated for ordinary percolation simulations. Ordinary percolation is suitable, for example, for liquid dropout at a dew point, or, for wetting fluid propagation through an irreducible network of near-surface films. Invasion percolation is more suitable for modeling flow in frontal displacement, where the nonwetting fluid is pushed into the pores while remaining connected to the inlet. The dashed relative permeability curves were computed from invasion percolation simulations assuming zero initial nonwetting fluid saturation. The presence of fracture in the sample shifts the relative permeability curves to the right, which means a higher permeability to the nonwetting fluid and a lower permeability to the wetting fluid.

The right-hand exhibits on Figures 9 and 11 show the relative permeability curves for the unfractured and fractured computer-generated media at contact angles $\theta = 30°$ and $\theta = 45°$, respectively. For both samples, simulations predict that wettability has a noticeably greater impact on the drainage relative permeability curves than the imbibition curves. This finding can be attributed to penetration of the nonwetting fluid into the matrix, which hinders access to the fracture for wetting fluid residing in matrix pores. The main implication for gas injection
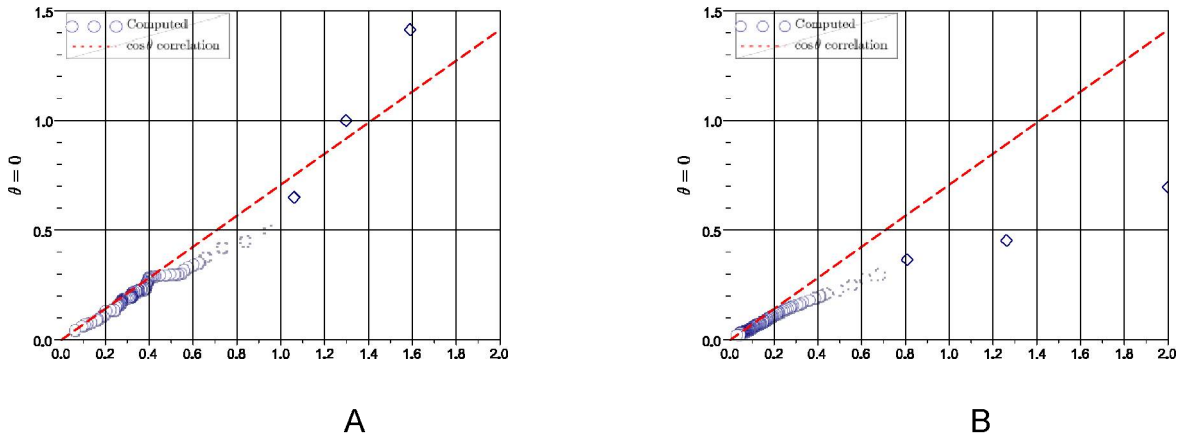
A   B

Figure 8. Examples of cos θ correlation and numerically evaluated capillary pressure. Both, for imbibition (A) and drainage (B) the correlation deviates from 1 at higher capillary pressures.
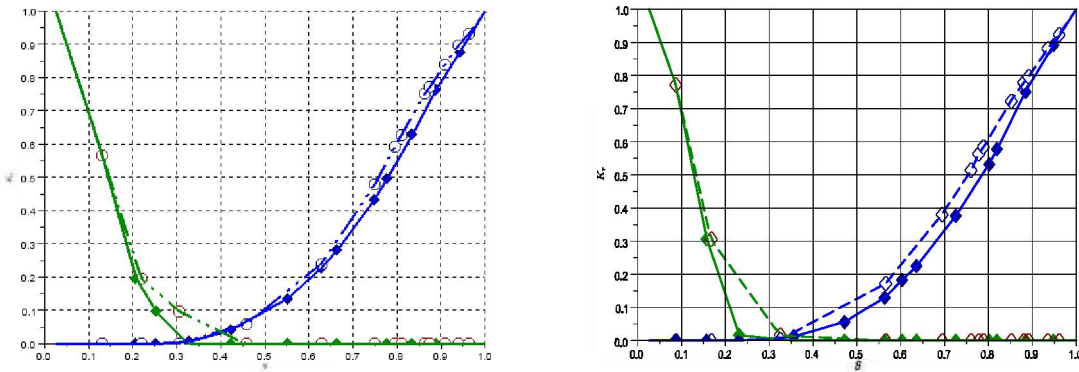

Figure 9. Relative permeability for unfractured computer-generated sample for zero (on the left) and 30° (on the right) degrees contact angles.

is that if the matrix blocks in fractured rock are large, it may take substantial time for the injected gas to reach the interior parts of the matrix blocks.

5. Conclusions

The main tool in this modeling study is a combination of MIS calculations with finite-difference flow simulations. MIS calculations have been extended to account for a non-zero contact angle by stretching each inscribed sphere and cutting disconnected voxels. Input data are digital 3D images of two computer-generated porous samples. The first sample mimics the geometry of a micro-CT image of Bentheimer sandstone. Capillary pressure curves computed for the computer-generated sample and digitized Bentheimer micro-CT data are in good agreement both for 0 ∘ and 45 ∘ contact angles. To imitate fracture, the grains of the computer-generated sample are parted along a fracture plane.
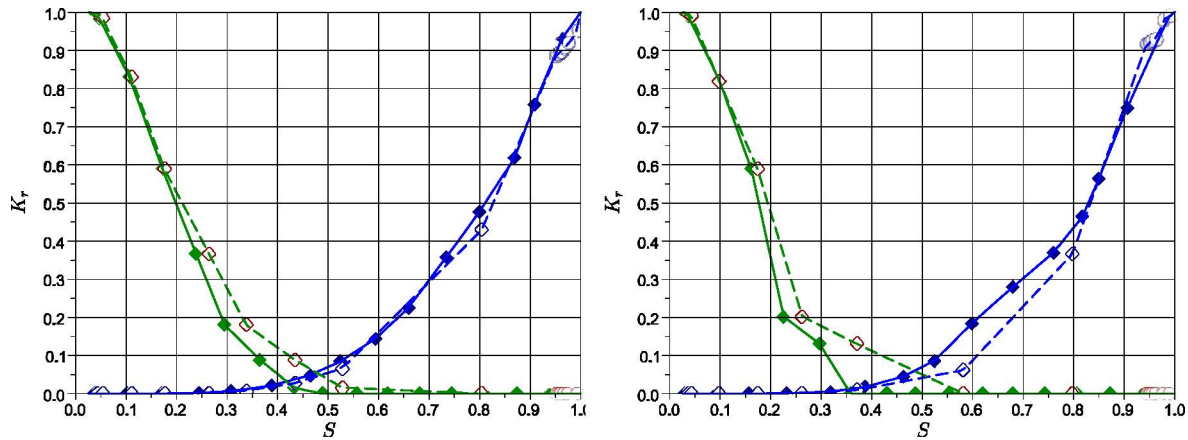
Simulations lead to the following observations:

Figure 10. Relative permeability curves evaluated from an image of Bentheimer sandstone assuming zero (on the left) and 45° (on the right) contact angles.
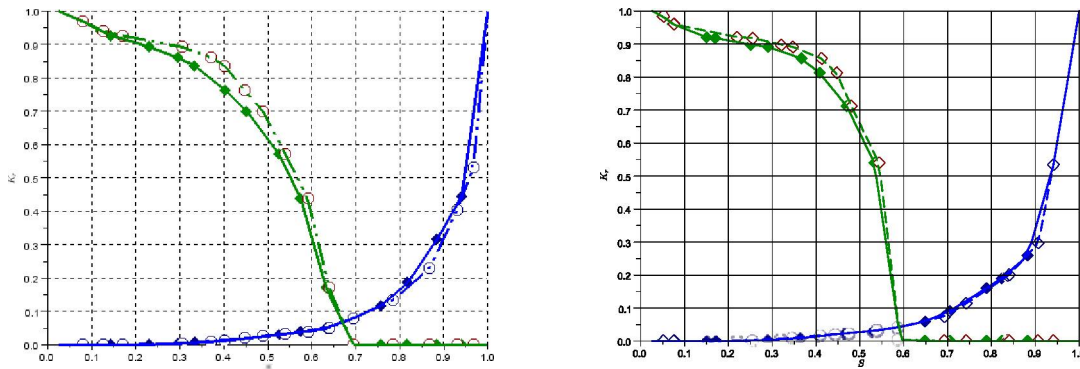

Figure 11. Relative permeability for computer-generated sample with fracture for zero (on the left) and 45° (on the right) degree contact angles.

- Both fracture and wettability have an impact on the two-phase properties of the rock and have to be accounted for in planning gas injection for geologic sequestration.
- Wettability alteration towards less hydrophilic solid reduces the capillary entry barrier. A fracture significantly enhances the relative permeability to gas and creates preferential gas flow paths.
- The impact of wettability on the relative permeability curves is less in the fractured-medium model than in the model rock sample with no fracture. Taking into account the low gas viscosity relative to the resident reservoir fluids, such preferential flow paths may stimulate the tendency of injected gas to bypass the bulk of matrix porosity.

The present study focuses on the interaction of flow and capillary equilibrium and does not account for other phenomena that may affect trapping or breakthrough of the injected gas. A more comprehensive study involving interaction of flow with geochemistry and geomechanics at different time and length scales will be needed for adequate planning of gas injection for the purpose of long-term geologic storage in a fractured reservoir.

6. Acknowledgments

References

1. W. G. Anderson, Wettability literature survey– Part 4: Effects of wettability on capillary pressure, Journal of Petroleum Technology 39 (1987), no. 10, 1283–1300.
2. Stig Bakke and Pål-Eric Øren, 3-D pore-scale modelling of sandstones and flow simulations in the pore networks, SPE Journal 2 (1997), 136–149.
3. C. B. Barber, D. P. Dobkin, and H. T. Huhdanpaa, The Quickhull algorithm for convex hulls, ACM Trans. on Mathematical Software 22 (1996), 469–483.
4. M. J. Blunt, Flow in porous media - pore-network models and multiphase flow, Current Opinion in Colloid & Interface Science 6 (2001), no. 3, 197–207.
5. A. J. Chorin, Numerical solution of the Navier–Stokes equations, Math. Comp. 22 (1968), 745–762.
6. I. Fatt, The network model of porous media. 1. Capillary pressure characteristics, Trans. AIME 207 (1956), no. 7, 144–159.
7. _____, The network model of porous media. 2. Dynamic properties of a single size tube network, Trans. AIME 207 (1956), no. 7, 160–163.
8. _____, The network model of porous media. 3. Dynamic propertries of networks with tube radius distribution, Trans. AIME 207 (1956), no. 7, 164–181.
9. O. I. Frette and J. O. Helland, A semi-analytical model for computation of capillary entry pressures and fluid configurations in uniformly-wet pore spaces from 2D rock images, Adv. Water Resources 33 (2010), no. 8, 846–866.
10. R. Holtzman, D. B. Silin, and T. W. Patzek, Mechanical properties of granular materials: A variational approach to grain-scale simulations, International Journal for Numerical and Analytical Methods in Geomechanics 33 (2009), no. 3, 391–404.
11. E. Jettestuen, J. O. Helland, and M. Prodanović, A variational level set method for simulation of capillary-controlled displacements, XIX International Conference on Water Resources CMWR June 17-22, 2012, University of Illinois at Urbana-Champaign, 2012.
12. G. Jin, T.W. Patzek, and D. B. Silin, Direct prediction of the absolute permeability of unconsolidated and consolidated reservoir rock. SPE 90084, 2003 SPE Annual Technical Conference and Exhibition (Houston, Texas, U.S.A.), SPE, 2004.
13. M. C. Leverett, Capillary behavior in porous solids, Trans. AIME 142 (1941), 152–169.
14. W. B. Lindquist and A. Venkatarangan, Investigating 3D geometry of porous media from high resolution images, Phys. Chem. Earth (A) 25 (1999), no. 7, 593–599.
15. F. S. Magnani, P. C. Philippi, Z. R. Liang, and C. P. Fernandes, Modelling two-phase equilibrium in three-dimensional porous microstructures, International Journal of Multiphase Flow 26 (2000), no. 1, 99–123.
16. M. Muskat, Physical principles of oil production, McGraw-Hill, New York, NY, 1949.

17. R. M. O'Connor and J. T. Fredrich, Microscale flow modelling in geologic materials, Physics and Chemistry of the Earth, Part A: Solid Earth and Geodesy 24 (1999), no. 7, 611–616.
18. P. E. Øren, S. Bakke, and H. G. Rueslätten, Digital core laboratory: Rock and flow properties derived from computer generated rocks, International Symposium of the Society of Core Analysts (Trondheim, Norway), Society of Core Analysits, 12-16 September 2006.
19. T. W. Patzek, Verification of a complete pore network simulator of drainage and imbibition, SPE Journal 6 (2001), no. 2, 144–156.
20. Maša Prodanović and Steven L. Bryant, A level set method for determining critical curvatures for drainage and imbibition, Journal of Colloid and Interface Science 304 (2006), no. 2, 442 – 458.
21. S. Rassenfoss, Digital rocks out to become a core technology, Journal of Petroleum Technology (2011), 36–41.
22. J. Schembre-McCabe, R. Salazar-Tio, G. Ball, and J. Kamath, A framework to validate digital rock technology. SCA2011-28, International Symposium of the Society of Core Analysts held in Austin, Texas, USA 18-21 September, 2011 , 2011.
23. D. Silin and T. Patzek, Pore space morphology analysis using maximal inscribed spheres, Physica A. Statistical Mechanics and its Applications 371 (2006), 336–360.
24. D. B. Silin, G. Jin, and T.W. Patzek, Robust determination of the pore-space morphology in sedimentary rocks. SPE 84296, 2003 SPE Annual Technical Conference and Exhibition (Denver, Colorado, U.S.A.), SPE, 2003.
25. D. B. Silin and T. W. Patzek, Predicting relative-permeability curves directly from rock images. SPE 124974, 2009 SPE Annual Technical Conference and Exhibition (New Orleans, Louisiana, U.S.A.), SPE, 2009.
26. Dmitriy Silin, Timothy J. Kneafsey, Jonathan B. Ajo-Franklin, and Peter Nico, A multi-modal 3D imaging study of natural gas flow in tight sands. SPE paper 146611, SPE Annual Technical Conference and Exhibition, 30 October-2 November 2011, Denver, Colorado, USA, 2011.
27. Dmitriy Silin, Liviu Tomutsa, Sally Benson, and Tad Patzek, Microtomography and pore-scale modeling of two-phase fluid distribution, Transport in Porous Media (2010), 1–21, 10.1007/s11242-010-9636-2.
28. Liviu Tomutsa, Dmitriy Silin, and Velimir Radmilovic, Analysis of chalk petrophysical properties by means of submicron-scale pore imaging and modeling, SPE Reservoir Evaluation and Engineering 10 (2007), no. 3, 285–293.

Earth Sciences Division, Ernest Orlando Lawrence Berkeley National Laboratory, 1 Cyclotron Road, Berkeley, CA, 94720, USA
E-mail address: DSilin@lbl.gov

Earth Sciences Division, Ernest Orlando Lawrence Berkeley National Laboratory, 1 Cyclotron Road, Berkeley, CA, 94720, USA
E-mail address: JBAjo-Franklin@lbl.gov

International Research Institute of Stavanger AS Postboks 8046, 4068, Stavanger, Norway
E-mail address: Johan.Olav.Helland@iris.no

International Research Institute of Stavanger AS Postboks 8046, 4068, Stavanger, Norway
E-mail address: Espen.Jettestuen@iris.no

International Research Institute of Stavanger AS Postboks 8046, 4068, Stavanger, Norway
E-mail address: Dimitrios.Hatzignatiou@iris.no

DISCLAIMER